High Power Laser Science and Engineering, (2020), Vol. 8, e7, 10 pages.
doi:10.1017/hpl.2020.5

HIGH POWER LASER SCIENCE AND ENGINEERING

RESEARCH ARTICLE

Hydrodynamic computational modelling and simulations of collisional shock waves in gas jet targets

Stylianos Passalidis[1,2], Oliver C. Ettlinger[2], George S. Hicks[2], Nicholas P. Dover[2,3], Zulfikar Najmudin[2], Emmanouil P. Benis[4], Evaggelos Kaselouris[1,5], Nektarios A. Papadogiannis[1,5], Michael Tatarakis[1,6], and Vasilis Dimitriou[1,5]

[1]*Institute of Plasma Physics & Lasers, Hellenic Mediterranean University, Chania 73133, Rethymno 74100, Greece*

[2]*The John Adams Institute, The Blackett Laboratory, Imperial College, London SW7 2AZ, UK*

[3]*Kansai Photon Science Institute, National Institutes for Quantum and Radiological Science and Technology (KPSI-QST), 8-1-7 Umemidai, Kizugawa, Kyoto 619-0215, Japan*

[4]*Department of Physics, University of Ioannina, GR Ioannina 45110, Greece*

[5]*Department of Music Technology and Acoustics, Hellenic Mediterranean University, Perivolia 74133, Rethymno, Greece*

[6]*Department of Electronic Engineering, Hellenic Mediterranean University, Chalepa 73133, Chania, Greece*

(Received 23 September 2019; revised 29 January 2020; accepted 7 February 2020)

Abstract

We study the optimization of collisionless shock acceleration of ions based on hydrodynamic modelling and simulations of collisional shock waves in gaseous targets. The models correspond to the specifications required for experiments with the CO_2 laser at the Accelerator Test Facility at Brookhaven National Laboratory and the Vulcan Petawatt system at Rutherford Appleton Laboratory. In both cases, a laser prepulse is simulated to interact with hydrogen gas jet targets. It is demonstrated that by controlling the pulse energy, the deposition position and the backing pressure, a blast wave suitable for generating nearly monoenergetic ion beams can be formed. Depending on the energy absorbed and the deposition position, an optimal temporal window can be determined for the acceleration considering both the necessary overdense state of plasma and the required short scale lengths for monoenergetic ion beam production.

Keywords: hydrodynamic simulations; ion acceleration; laser–plasma interaction

1. Introduction

Over the past 15 years, the generation of multi-MeV proton and ion beams with unique properties has attracted intense interest due to the numerous fundamental and applicative prospects these beams offer[1–5]. The mechanism proposed here constitutes a novel laser driven ion acceleration scheme[2] that offers greater control on the energy of the ions. In this mechanism, ions are accelerated by being pushed by the potential barrier located at a collisionless shock front generated by the laser source[2, 6–9].

Although in most previous studies of ion acceleration solid targets are used, gas targets may provide debris-free acceleration and a reduction of unnecessary secondary radiation, such as bremsstrahlung. Gas jets are also considered as sources of high-purity high-Z (e.g., Kr, Xe) ion beams and thus are considered as an alternative to solid foils. Gas jets are easily replenished targets, as opposed to foils, operating at high-repetition rates and offering controllable material properties[10]. The main disadvantage, however, is the difficulty to reach densities higher than the critical density, which is necessary for efficient ion acceleration, e.g., for 1 μm laser wavelength, $n_c \approx 10^{21}$ cm^{-3}[11, 12]. A way to overcome this obstacle is by using longer wavelength lasers. For example, for an infrared CO_2 laser with a wavelength of approximately 10 μm, the critical density is $n_c(\propto \lambda^{-2}) \approx 10^{19}$ cm^{-3}. This density is easily obtained by the ionization of gas targets via a prepulse.

The generation and subsequent properties of shock accelerated ion beams are highly dependent on the initial plasma density distribution[13–15]. In experiments performed using intense CO_2 lasers, it is surmised that the profile is modified by a pulse train inherent to the laser system[15, 16],

Correspondence to: V. Dimitriou, Institute of Plasma Physics & Lasers, Hellenic Mediterranean University, Chania 73133, Rethymno 74100, Greece. Email: dimvasi@hmu.gr

which varies from shot to shot, thus making the interactions challenging to reproduce. A technique to overcome this problem is the preparation of the gas target by an optically generated hydrodynamic blast wave from a lower energy laser prepulse. Such a method, where two different pulses are used to accelerate ions, has been recently demonstrated[17]. Considering an opaque and near-critical initial density, the lower energy prepulse forms a blast wave with steepened particle density, thus resulting in an overcritical density. After a few nanoseconds, the second and high energy main pulse accelerates the ions at the front of the shock[17].

In the present study, which is based on the work of Tresca *et al.*[17], the hydrodynamic expansion of the blast wave due to the prepulse and corresponding density is computationally studied for parameters relevant to the specifications of the two aforementioned lasers. This research is focused only on the hydrodynamic expansion stage and not on the heating stage from the laser[14]. The absorption efficiency and spatial profile could be affected nonlinearly by the prepulse energy, but the laser plasma absorption mechanism studies are beyond the scope of this work. The hydrodynamic simulation results demonstrate that by controlling the laser pulse energy, the deposition position and the backing pressure, a blast wave suitable for studying collisionless shock acceleration can be formed. The proposed model is purely hydrodynamic, with low computational power demands, since it does not include heat conduction and ion viscosity or ionization on the blast wave front. To extend the findings of previous research works, we explore new conditions including scanning of the initial density and the energy deposited, for two different wavelength regimes (Brookhaven National Laboratory (BNL) and Vulcan), using an existing and benchmarked model[14, 17]. This will help future experiments determine the plasma heating requirements for generating density profiles favourable for quasimonoenergetic ion beam generation.

Considering the case of the BNL CO_2, for three different densities of the gas, four different absorbed energy values and deposition positions varying from 0.02 to 0.1 cm from the axis of the jet are simulated. These models are also used to simulate the case of the Vulcan laser system for the study of six different absorbed energy values. The spatiotemporal evolution of the particle densities corresponding to various pulse energies, laser focal positions and backing pressures is compared to optimize the steepened density gradients of the blast wave walls. The computational results of these simulations provide valuable data leading to optimization of the jets and the laser systems used in experiments and simulations that focus on particle acceleration.

2. Physical modelling

In the first stage of the laser–gas interaction, the main mechanism of energy absorption is the inverse bremsstrahlung heating. Electrons gain energy from the incident optical high power laser pulse via collisions. At a very high field strength, gases break down, i.e., they become highly ionized, accompanied by a light flash. The electron–ion collision frequency is given by[18, 19]

$$\begin{aligned} \upsilon_{\mathrm{ei}} &= \frac{1}{3(2\pi)^{3/2}} \frac{n_e Z e^4 \ln \Lambda}{\varepsilon_0^2 m_e^{1/2} (k_b T_e[\mathrm{K}])^{3/2}} \\ &\approx \frac{2.9 \times 10^{-12} n_e Z[\mathrm{m}^{-3}]}{(T_e[\mathrm{eV}])^{3/2}} \ln \Lambda, \end{aligned} \tag{1}$$

where n_e is the plasma electron density, Z is the atomic number, k_b is the Boltzmann constant, T_e is the electron temperature and $\ln \Lambda$ is the Coulomb logarithm. The free electron density depends on the ionization fraction, which is dynamic as an increasing amount of energy is absorbed in the plasma. The absorption coefficient for inverse bremsstrahlung is given by

$$K = \frac{\upsilon_{\mathrm{ei}}}{c} \left(\frac{n_e}{n_c}\right) \left(1 - \frac{n_e}{n_c}\right)^{-1/2}, \tag{2}$$

where n_c is the critical electron density. The corresponding fraction of the laser energy thermally absorbed by the plasma is

$$\eta \approx 1 - \exp(-K Z_R), \tag{3}$$

where Z_R is the Rayleigh length. For a few ps pulse duration, the hydrodynamic expansion of the plasma is negligible. Considering that the heating is uniform inside the cylindrical volume defined by the beam waist w_0 and twice the Rayleigh length Z_R, then for hydrogen ($Z = 1$), the plasma temperature due to the laser heating is given by[14]

$$T_e(t)[\mathrm{eV}] = \frac{1}{2 n_e Z_R e} \int_0^t I_L \{1 - \exp[-K(t) Z_R]\} \, \mathrm{d}t. \tag{4}$$

In the frame of the present work, after the initial energy deposition, the heated plasma hydrodynamically expands into the surrounding ambient medium as a blast wave in a similar way to the Sedov or adiabatic stage of supernova or atomic explosions[20–22]. The hydrodynamic code FLASH, created by the Flash Center for Computational Science at the University of Chicago, has been used to simulate the interaction of a laser pulse with an ambient hydrogen gas target, having an initial density approximately above 0.5×10^{17} cm^{-3}. The 1 mJ energy of the BNL CO_2 prepulse is deposited in the gas target, and, thus, a blast wave is formed that expands in the ambient medium, as presented in Figure 1. Gas is accumulated on the walls of the shock resulting in a six times higher density, as compared to the initial density, forming a cavity at the centre. This compression factor depends on the composition of the gas

https://doi.org/10.1017/hpl.2020.5 Published online by Cambridge University Press

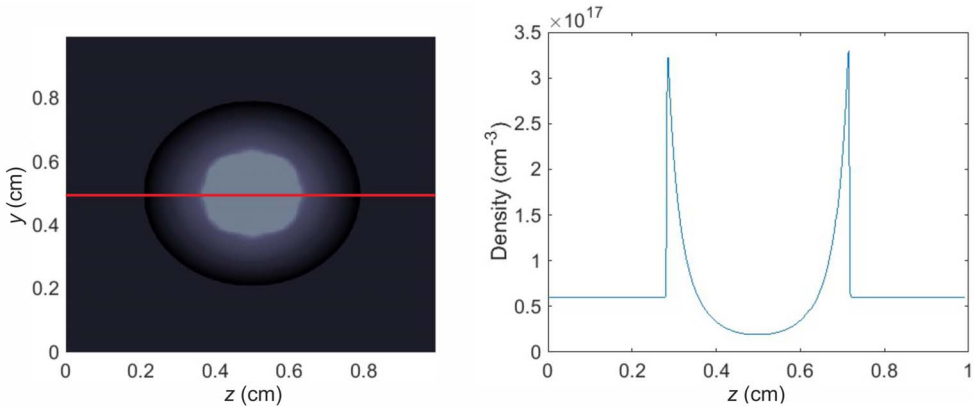

Figure 1. Simulation of the spherical expansion of the blast wave (left) and the lineout (red line) of the steep density walls at the front of the shock (right) in an homogeneous hydrogen gas, for initial density of 0.5×10^{17} cm^{-3} and 1 mJ absorbed energy of the BNL CO_2 laser.

of the medium since the collisionality differs for various elements. When the blast shock wave is strongly driven, the equations of motion follow the self-similar Sedov solution presented below[20].

The expansion velocity $u_{\rm sh}(r,t)$, density $\rho(r,t)$, pressure $p(r,t)$ and other properties of a blast wave are determined solely by two parameters of the system, the absorbed energy $E_{\rm abs}$ and the initial density ρ_0, by the Sedov self-similar solution. The radius of the blast wave is given by

$$r_{\rm bw}(t) = \zeta_0(\gamma)\left(\frac{E_{\rm abs}}{\rho}\right)^{1/(2+\alpha)} t^{2/(2+\alpha)}, \qquad (5)$$

where $\alpha = 1, 2, 3$ is the dimensionality of the shock for a shock having a plane, cylindrical or spherical symmetry respectively, ρ is the mass density of the ambient gas and $\zeta_0(\gamma)$ is a numerical constant of order unity[21].

The expansion rate of the shock is described by

$$u_{\rm sh} = \frac{{\rm d}r(t)}{{\rm d}t} = \frac{2}{2+a}\zeta_0(\gamma)\left(\frac{E_{\rm abs}}{\rho}\right)^{1/(2+a)} t^{2/(2+a)-1}. \qquad (6)$$

By solving Equation (5) for the variable t and by introducing it in Equation (6), the expansion rate of the shock may be described by

$$u_{\rm sh} = \frac{2}{2+a}[\zeta_0(\gamma)]^{(2+a)/2}\left(\frac{E_{\rm abs}}{\rho}\right)^{1/2} r^{-a/2}. \qquad (7)$$

The velocity of the shock is $\propto r^{-1/2}$, $\propto r^{-1}$ and $\propto r^{-3/2}$ for the plane, cylindrical and spherical cases, respectively, which means that the velocity reduces as the shock wave expands. The self-similar blast wave solution is not valid for the whole expansion duration; for instance, at $t \to 0$, the solution approaches an infinite expansion rate.

The density scale length is a parameter of major importance in controlling the properties of accelerated ions and is the distance over which the density decreases by a factor of e. A steep initial front surface plasma density scale length is crucial not only to achieve shock acceleration but also for the spectral control of the ion beam. It has been observed that long density gradients in hydrogen plasmas lead to the production of broadband shock accelerated ion beams, while steeper gradients allow for the generation of quasimonoenergetic beams as explained in Refs. [17, 23].

The density profiles of a blast wave, corresponding to the BNL CO_2 laser at 4 bar initial pressure and absorbed energy of $E = 20$ mJ along the laser propagation axis, are presented in Figure 2. The laser beam is focused close to the exit of the nozzle (i.e., at $y \approx 0$ and $z = -0.02$ cm; see Figure 2 inset). At these heights above the nozzle exit, it has been shown that the density profile can be approximated by a triangle[24]. The density profiles of a shock for $t = 0$, 1, 12 and 20 ns are shown. The blast wave is seen to expand and most of the density is accumulated at the walls. The absence of symmetry is due to the deposition of energy away from the centre of the gas jet along the z-axis. It is evident that the right side of the blast wave, which has propagated through the centre of the gas, accumulates sequentially more particles, thus resulting in a higher shock wall density, shown by the right red curve. Furthermore, it is seen that the scale length increases with increasing time. The density profile is very sharp in the first nanosecond of the production of the shock (right red curve). After 11 ns, it becomes less steep (yellow curve), and finally after 20 ns, it has widened in space noticeably (purple curve).

3. Numerical modelling

The modular, parallel, multiphysics simulation code FLASH was used for our simulations[25]. FLASH handles general compressible flow problems by solving the Euler equations

https://doi.org/10.1017/hpl.2020.5 Published online by Cambridge University Press

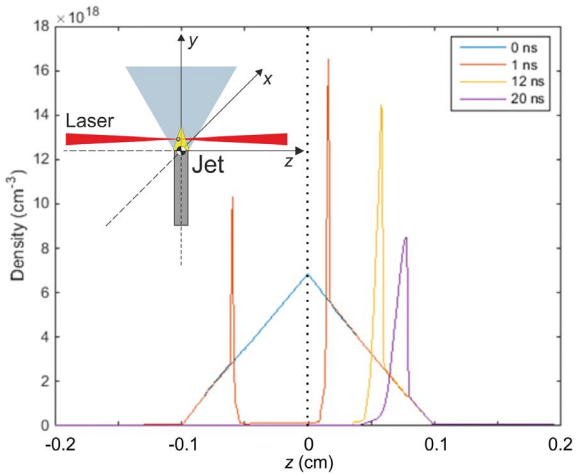

Figure 2. Time evolution of density profiles along the laser propagation axis for a blast wave at $t = 0$, 1, 12 and 20 ns, corresponding to the BNL CO_2 laser, at 4 bar initial pressure and absorbed energy 20 mJ. The laser beam is focused at $z = -0.02$ cm.

for compressible gas dynamics, expressed in the conservative form:

$$\begin{aligned} &\frac{\partial \rho}{\partial t} + \vec{\nabla} \cdot \left(\rho \vec{v}\right) = 0, \\ &\frac{\partial \rho \vec{v}}{\partial t} + \vec{\nabla} \cdot \left(\rho \vec{v}\,\vec{v}\right) + \vec{\nabla} P = \rho \vec{g}, \\ &\frac{\partial \rho E}{\partial t} + \vec{\nabla} \cdot \left[(\rho E + P)\vec{v}\right] + \vec{\nabla} P = \rho \vec{v} \cdot \vec{g}, \end{aligned} \tag{8}$$

where ρ is the fluid density, $\vec{v}$ is the fluid velocity, P is the pressure, E is the sum of the internal energy ε and kinetic energy per unit mass, $E = \varepsilon + \frac{1}{2}v^2$, and g is the gravity acceleration. The pressure is obtained from the energy and density using the equation of state:

$$P = (\gamma - 1)\rho\varepsilon. \tag{9}$$

This partial differential equation system of the Euler equations is solved using an unsplit hydrodynamic solver with third-order interpolation which corresponds to the piecewise parabolic method (PPM). The PPM scheme is a higher-order extension of Godunov's method[26, 27] that uses a finite-volume spatial discretization of the Euler equations, combined with an explicit forward time difference. This solution scheme was introduced by van Leer in the MUSCL (Monotonic Upstream-centered Scheme for Conservation Laws) algorithm[28, 29]. The PPM scheme provides a substantial advance over MUSCL in several aspects[30]. The introduction of parabolic fits as basic interpolation functions in a zone allows for a more accurate representation of smooth spatial gradients as well as a steeper representation of the captured discontinuities and particularly the contact discontinuities. The representation of the nonlinear wave interactions used to compute fluxes is substantially simpler than the one used in MUSCL, thus providing a less complicated and robust algorithm.

A major advantage of the FLASH code is that the simulation domain is discretized and refined by the help of an adaptively mesh refined (AMR) grid. The application of AMR grid is based on an initial Eulerian grid where the regions that require finer resolution are identified and finer sub-grids (extra computational cells) are generated. This refinement process is controlled by the help of a local truncation error estimator[25].

FLASH includes two AMR algorithms, the default PARAMESH package that was used in our study and CHOMBO[31] that uses a block-structured adaptive mesh refinement scheme[32–34]. The complete computational grid consists of a collection of blocks with different physical cell sizes, which are related to each other in a hierarchical way using a tree data structure. The blocks at the root of the tree include the big cells (parents), while their children have smaller cells and are further refined[20].

4. Numerical hydrodynamic simulations

An analytic model developed for this study is based on a customized version of the Sedov model, as described in detail in Ref. [14]. The advantage of cylindrical symmetry is used for the 2D model, as proposed in Ref. [14], and the energy deposition is numerically defined by the beam waist and the Rayleigh length to form a cylinder representing the confocal volume of the beam as shown in the left of Figure 3. The test case of the CO_2 laser at BNL is studied. The beam waist radius is $w_0 = 35$ μm and the corresponding Rayleigh length is $Z_R = 374$ μm. At $t = 0$, the beam is focused at $z = -0.06$ cm, as schematically depicted in the inset of Figure 2. The ambient pressure of the chamber, the initial gas pressure and temperature as well as the nozzle length, throat and exit diameters can be defined accordingly.

The boundary conditions are reflecting on the axis of the cylinder, on the left of the domain, to model the cylindrical symmetry. Outflow boundary conditions (zero-gradient boundary conditions) are applied to the rest of the three sides, allowing shocks to leave the computational domain without any reflections.

As depicted in the right part of Figure 3, when the blast wave propagates along the positive direction of the z-axis, the front of the wave meets dense gas. On the contrary, the back of the blast wave has already reached the edge of the jet's cone and starts to deform in the ambient gas. By taking advantage of the cylindrical symmetry, the zy symmetric cross-section plane of the blast wave is simulated and presented.

Alongside with the initial conditions of the numerical problem, the throat and exit diameters as well as the length of

https://doi.org/10.1017/hpl.2020.5 Published online by Cambridge University Press

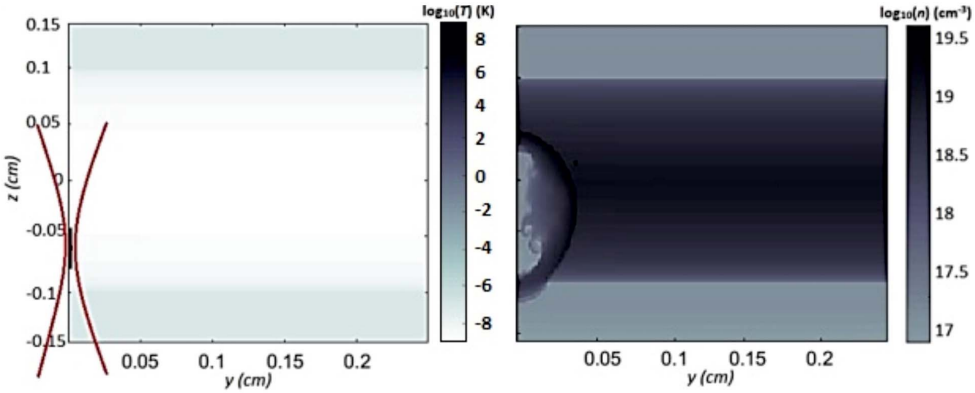

Figure 3. Left: the cylinder where the energy is deposited, representing the confocal volume of the laser pulse with $w_0 = 35$ μm and $Z_R = 374$ μm. At $t = 0$, the beam is focused at $z = -0.06$ cm along the laser propagation axis (z-axis) along the direction of the gas flow (y-axis). Right: the formation of the blast wave at $t = 4$ ns corresponding to the CO_2 specifications, at 4 bar initial pressure and absorbed energy 100 mJ, deposited at $z = -0.02$ cm.

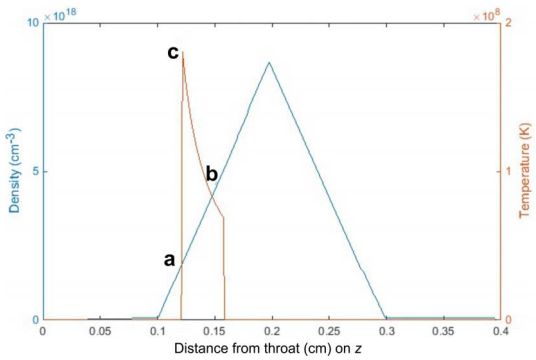

Figure 4. The triangular density shape used in the simulation (blue) and the initial energy deposition (red), for $w_0 = 35$ μm, $Z_R = 374$ μm and $E_{abs} = 10$ mJ.

the nozzle are set. The nozzle simulated is a so called '1 mm' nozzle, with a throat diameter of 0.5 mm, an exit diameter of 1 mm and length of 4 mm. The longitudinal density profile can be approximated as a triangle[24]. This triangular shape used in the simulations in this study, as well as the initial energy deposition, is shown in Figure 4. The deposition of the energy across the focal volume is considered homogeneous. The trapezoidal shape of the energy deposition (red line) ensures that the initial energy is deposited homogeneously across the deposition satisfying the following equation:

$$n_a k_B T_c = n_b k_B T_b, \tag{10}$$

where a, b and c subscripts correspond to the points in Figure 4.

The initial grid of cells that models the computational domain for all of the simulations performed had an initial uniform discretization of 42 × 8 cells, in the X and Y directions, respectively, with a starting size of 0.05 cm × 0.04 cm. The eighth order (up to the eighth child cell) of the maximum refinement scheme is always used, which leads to the refined cells selected by AMR sub-domains, to a minimum cell size of 3.91×10^{-4} to 3.12×10^{-4} cm. The simulations were performed on the CX1 Cluster of Imperial College London, on one node of 16 cores and 14 GB memory[35]. On CX1, the simulation runtimes range from 5 min up to the maximum of 30 min, even for the most time-consuming cases. In order to keep the wall clock time of the simulation runtimes within this time range, the discretization parameters for all of the models was kept constant. The resulting course domain discretization is responsible for the lack of smoothness of the resulting curves that represent the ratio of the peak electron density to the critical density, in Figures 7–9.

5. Results and discussion

5.1. BNL CO_2 case

The simulations performed focused on the investigation of the density profiles of the blast waves and the determination of the time over which the main pulse irradiates the overdense plasma. The FLASH code is set to output data files at every nanosecond simulated, the wavelength to $\lambda = 10.3$ μm and the critical density to $n_c = 9.99 \times 10^{18}$ cm^{-3}. The profile of the molecular density distribution for the three gas jet densities at BNL is presented in Figure 5. Three initial molecular densities of $n = 3.39 \times 10^{18}$ cm^{-3}, $n = 4.42 \times 10^{18}$ cm^{-3} and $n = 5.09 \times 10^{18}$ cm^{-3} (that correspond to 0.34, 0.44, 0.51 of n_c for 4, 5, 6 bar of backing pressure, respectively) were tested using the FLASH code for the gas jet simulations, for four absorbed energies in the range of 0.1–100 mJ and five laser focused areas in the range of 0.1–0.02 cm away from the centre (z-axis) of the jet. The nozzle characterization was performed at Imperial College using a Mach–Zehnder interferometer setup. For our simulations,

https://doi.org/10.1017/hpl.2020.5 Published online by Cambridge University Press

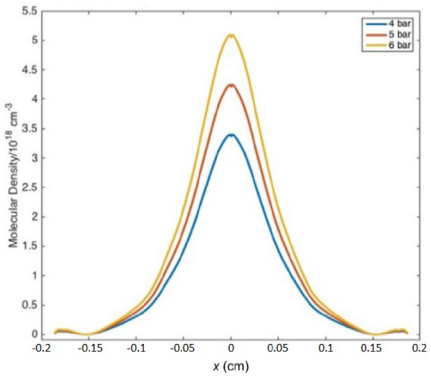

Figure 5. The profiles of backing pressures of 4, 5 and 6 bar (maximum) that correspond to the molecular densities of $n = 3.39 \times 10^{18}$ cm^{-3}, $n = 4.42 \times 10^{18}$ cm^{-3} and $n = 5.09 \times 10^{18}$ cm^{-3}, respectively.

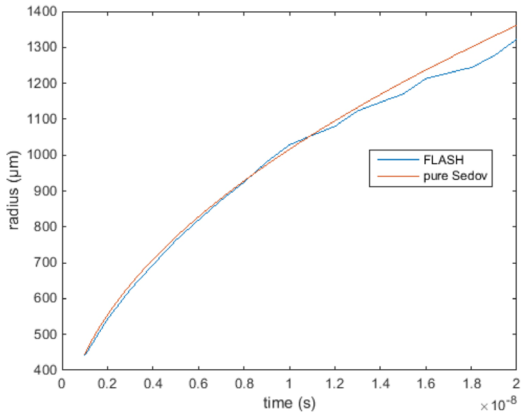

Figure 6. Comparison of the FLASH and self-similar Sedov results for 20 mJ absorbed energy, for initial density $n = 3.39 \times 10^{18}$ cm^{-3}, deposited at 0.02 cm prior to the centre of the throat.

these molecular density profiles ensure that the maximum density used is under the peak value of these profiles.

A comparison example for the case of $E_{\text{abs}} = 20$ mJ deposited at 0.02 cm prior to the centre of the throat and $n = 3.39 \times 10^{18}$ cm^{-3} is demonstrated in Figure 6. The radius that corresponds to the position of the front of the shock in the laser propagation axis (i.e., z-axis) is presented. It follows Equation (5), taking into account the correction for the changing density. As it can be clearly seen, the FLASH numerical and the analytical results of the Sedov-based model[14] are in a good agreement.

Following this, four energies of 1, 5, 20 and 100 mJ were studied. The results of the blast wave radii and the corresponding ratio of the peak electron density to the critical density are presented in Figure 7 for a backing pressure of 4 bar. The electron density that corresponds to twice the molecular density is adopted.

The time frame within which the main pulse interacts with the target is highly dependent on the region where the prepulse is focused. In Figure 7 (right), it is shown that for lower energies and deposition position 0.1 cm from the jet's throat, few nanoseconds are necessary until the plasma density exceeds the critical value. Thus, in this case, the critical density can be overcome very easily in the first nanoseconds after the prepulse–plasma interaction, and the production of large density scale lengths can be avoided for the generation of monoenergetic accelerated ion beams.

On the contrary, if we deposit the energy very close to the jet's throttle, there is the risk of never creating an overdense plasma, especially for high pulse energies, as shown in Figure 8. Indeed, at higher energies and deposition positions close to the throat of the jet, the density decreased very fast because it is possible to move below the critical density since the shock wave moves towards the descending side of the density's ramp, thus resulting in undercritical density gradients even in the blast wave's walls (Figure 8 (right)). In this case, the main pulse should be applied right after the prepulse. For example, in case the energy deposition position is very close to the throat, e.g., at 0.02 cm away from it, the 100 mJ prepulse reached the peak of the initial density ramp and the peak density on the wall of the blast wave started to descend intensively. At the same time, the blast waves produced by lower laser energies move slower, are still in the region where they steadily absorb mass from the front of the shock and remain at the same high densities above the critical value.

The main conclusion from the above results is that for lower, medium and high laser pulse energies, the target is overcritical. Hence, there is no necessity to apply the main pulse at later times having to deal with unnecessary long density scale lengths. Hydrogen would be a good choice for these experiments. In earlier works where helium was used[10], it was found to be harder to produce overcritical plasma at such early time after the prepulse interaction with the gas.

It is of great importance that the scale length values, for the three energies, are relatively low and permit the production of monoenergetic ion beams since scale lengths lower than 40 μm have been shown to be favourable for the acceleration of quasimonoenergetic ion beams[17, 23]. This scale length L, which defines the shock thickness, is calculated from the FLASH simulations by the fitting of an exponential of the form $n = n_0 e^{-x/L}$ to the density gradient at the target front surface. For this laser system with 10.6 μm wavelength and a hydrogen gas target, the density increases to exceed the plasma critical density before the blast wave scale length L exceeds the value of 20 μm, thus providing conditions favourable for the acceleration of quasimonoenergetic ion beams. In Figure 9, the evolution of the scale length versus time (left) and blast wave radii (right) for density $n = 4.42 \times 10^{18}$ cm^{-3} and 5, 20 and 100 mJ absorbed energies are presented, starting from 1 ns after the start of the simulation, where the blast wave has reached the self-similar stage, together with a polynomial fit to the simulation output. As can be seen in Figure 9 (right), the self-similarity of the blast wave expansion results in the scale length being determined

https://doi.org/10.1017/hpl.2020.5 Published online by Cambridge University Press

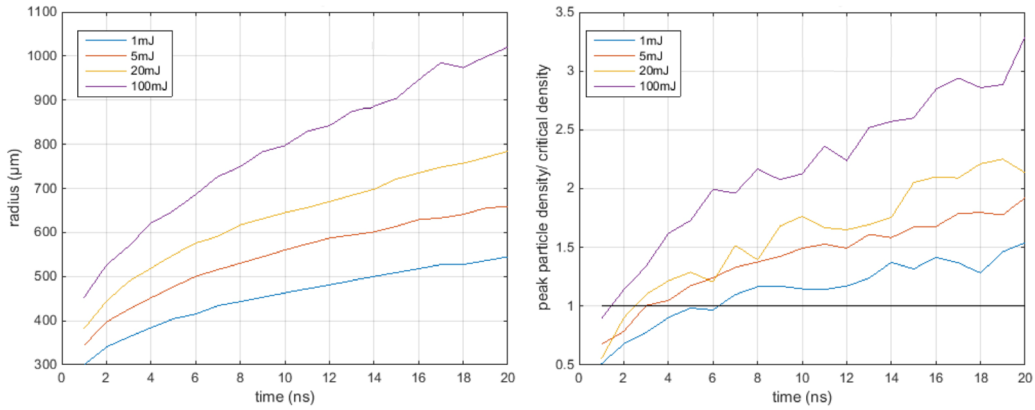

Figure 7. The blast wave radii (left) and the corresponding ratio of the peak electron density to the critical density (right). Time evolution up to 20 ns for 1, 5, 20 and 100 mJ absorbed energy deposited at $z = 0.1$ cm prior to the centre of the throat. Initial density was set to $n = 3.39 \times 10^{18}$ cm^{-3}.

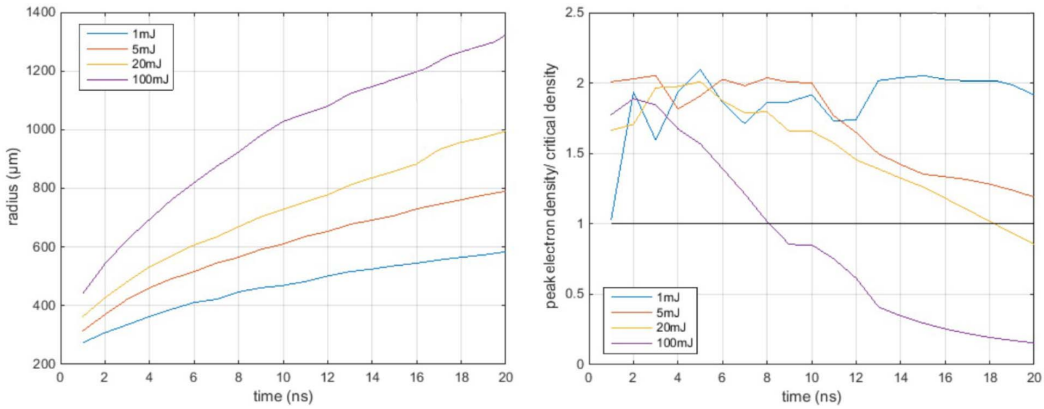

Figure 8. The blast wave radii (left) and the corresponding ratio of the peak electron density to the critical density (right). Time evolution up to 20 ns for 1, 5, 20 and 100 mJ absorbed energy deposited at 0.02 cm prior to the centre of the throat. Initial density was set to $n = 3.39 \times 10^{18}$ cm^{-3}.

by the blast wave radius, independent of the absorbed energy and expansion time.

5.2. Vulcan laser

The simulation results for targets suitable for experiments using the Vulcan laser at Rutherford Appleton Laboratory are presented here. The FLASH code is set again to output data files at every nanosecond simulated, the wavelength to $\lambda = 1053$ nm, and the beam waist to $w_0 = 5$ μm resulting in a Rayleigh length of 74.6 μm and a critical density $n_c = 1.01 \times 10^{21}$ cm^{-3}.

A maximum initial electron density of $n = 4.52 \times 10^{20}$ cm^{-3} (corresponding to 0.45 of n_c) is used in the simulations, equivalent to a standard gas jet with a backing pressure of ∼180 bar. In Figure 10, the simulated evolution of the radii of the blast waves is presented for six absorbed energies from 5 mJ to 1 J.

The time evolution for the ratio of the peak electron density to the critical density in the shock is presented in Figure 10 (right). Comparing the obtained results from both laser systems, it is important to note that it is harder to achieve critical density using the 1053 nm wavelength Vulcan laser. The critical density increases to 10^{21} cm^{-3} meaning that a very high initial density must be used, leading to a requirement for extremely high backing pressures for the gas jet. Even for this initial density, the density of the shock exceeds the critical density only after many nanoseconds. Only for high absorbed energy values, such as 250 mJ, 500 mJ and 1 J, could the density exceed critical density within 5 ns.

Following the same concept of the results visualization used for the BNL case in Figure 9, the scale lengths versus time for the Vulcan laser system are depicted in Figure 11. It is observed that the scale lengths of the density of the blast wave are lower than 40 μm. Although the scale length requirements for quasimonoenergetic ion acceleration with a lower wavelength, 1 μm, have still not been identified experimentally, it is likely that, similarly to longer wavelengths, short scale lengths will be required.

https://doi.org/10.1017/hpl.2020.5 Published online by Cambridge University Press

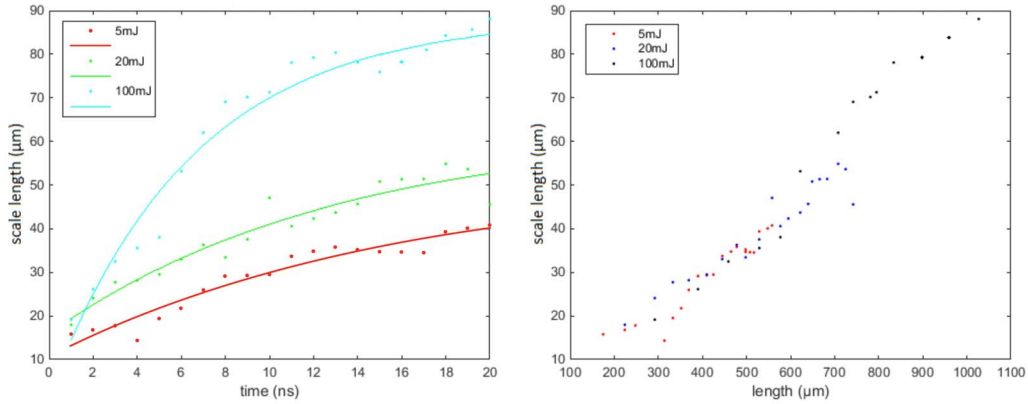

Figure 9. The density scale lengths versus time (left) and blast wave radii length (right), for density of $n = 4.42 \times 10^{18}$ cm^{-3} and absorbed energies of 5, 20 and 100 mJ.

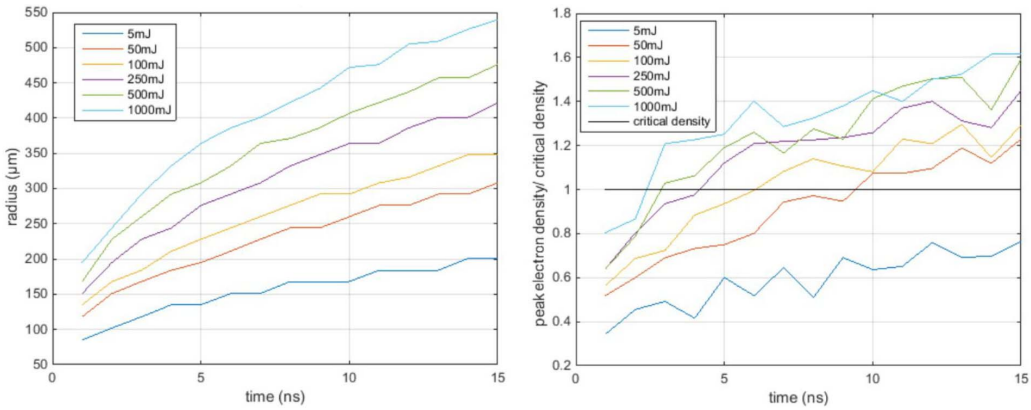

Figure 10. The blast wave radii (left) and the corresponding ratio of peak electron density to the critical density (right). Time evolution up to 15 ns for 5, 50, 100, 250, 500 and 1000 mJ absorbed energies, deposited at 0.05 cm prior to the centre of the throat. Initial density was set to $n = 4.52 \times 10^{20}$ cm^{-3}.

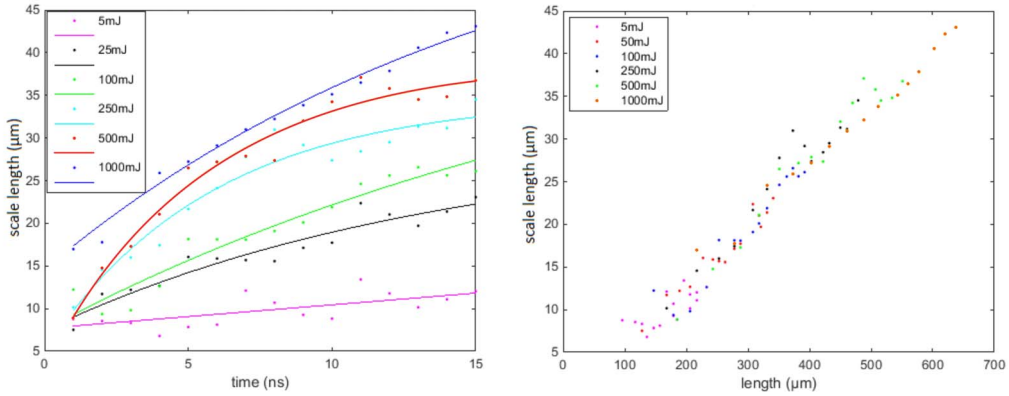

Figure 11. The density scale lengths versus time (left) and blast wave radii length (right), for density of $n = 4.52 \times 10^{21}$ cm^{-3} and absorbed energies of 5, 50, 100, 250, 500 and 1000 mJ.

6. Conclusions

The use of a lower energy prepulse to create a blast wave in the gas jet, thus shaping the target, has been proposed in the literature. Following the prepulse, the higher energy main pulse finds a sharpened density gradient that facilitates ion acceleration[14, 15, 17]. It is thought that the sharper the density gradient the more monochromatic the accelerated

https://doi.org/10.1017/hpl.2020.5 Published online by Cambridge University Press

ion beam. The aim of this study was to examine whether the time windows within overcritical plasma densities can be achieved, thus favouring collisionless shock acceleration of ions.

The critical plasma density is highly dependent on the laser wavelength. We chose to investigate these two particular laser systems, BNL CO_2 $\sim$ 10 μm and Vulcan $\sim$1 μm with wavelengths that differ one order of magnitude, to emphasize the difficulty to reach critical density when using laser of smaller λ. Comparing the obtained simulation results from the two laser systems, for the case of the 10.3 μm CO_2 laser, overcritical densities may be achieved even for absorbed energies as low as 1 mJ. In all the simulations involving hydrogen, even when 4 bar of backing pressure was used, the critical density can be reached within the first nanosecond. In addition, it was observed that using high energy pulses focused close to the centre of the jet, it is possible to move below the critical density since the shock wave moves towards the descending side of the density's ramp. For near μm laser drivers, such as the Vulcan laser, it is observed that it is harder to achieve the critical density for the 1053 nm wavelength. At this wavelength, the critical density of 10^{21} cm^{-3}, corresponding to backing pressure of 180 bar, must be used. Even for this initial density, only the density gradients of the shock overcome the critical one after many nanoseconds. Only high value absorbed energies can overcome this limit in less than 5 ns.

The analysis of the variables of interest indicates that, depending on the energy absorbed and the deposition position, gas targets can be shaped suitably and thus an identical temporal window may be determined for the acceleration considering both the necessary overdense state of plasma and the required short scale lengths for monoenergetic ion beams. The new simulation results offer valuable data for the optimization of future experiments since new conditions including scanning of the initial density and energy deposited for two different wavelength regimes have been explored here. This will help future experiments determine the plasma heating requirements for generating density profiles favourable for quasimonoenergetic ion beam generation.

Acknowledgements

The software used in this work was in part developed by the DOE NNSA-ASC OASCR Flash Center at the University of Chicago. IPPL authors acknowledge support of this work by the project 'ELI - LASERLAB Europe Synergy, HiPER & IPERION-CH.gr' (MIS 5002735) which is implemented under the Action 'Reinforcement of the Research and Innovation Infrastructure', funded by the Operational Programme 'Competitiveness, Entrepreneurship and Innovation' (NSRF 2014-2020) and co-financed by Greece and the European Union (European Regional Development Fund).

References

1. S. C. Wilks, W. L. Kruer, M. Tabak, and A. B. Langdon, Phys. Rev. Lett. **69**, 1383 (1992).
2. L. O. Silva, M. Marti, J. R. Davies, R. A. Fonseca, C. Ren, F. S. Tsung, and W. B. Mori, Phys. Rev. Lett. **92**, 015002 (2004).
3. M. Borghesi, Nucl. Instrum. Methods Phys. Res. **740**, 6 (2014).
4. S. V. Bulanov, T. Zh Esirkepov, V. S. Khoroshkov, A. V. Kuznetsov, and F. Pegoraro, Phys. Lett. A **299**, 240 (2002).
5. M. Kaluza, J. Schreiber, M. I. Santala, G. D. Tsakiris, K. Eidmann, J. Meyer-ter-Vehn, and K. J. Witte, Phys. Rev. Lett. **93**, 045003 (2004).
6. M. Q. He, Q. L. Dong, Z. M. Sheng, S. M. Weng, M. Chen, H. C. Wu, and J. Zhang, Phys. Rev. E **76**, 035402 (2007).
7. M. Chen, Z. M. Sheng, Q. L. Dong, M. Q. He, Y. T. Li, M. A. Bari, and J. Zhang, Phys. Plasmas **14**, 053102 (2007).
8. A. Henig, D. Kiefer, M. Geissler, S. G. Rykovanov, R. Ramis, R. Hörlein, and F. Krausz, Phys. Rev. Lett. **102**, 095002 (2009).
9. P. Antici, E. Boella, S. N. Chen, D. S. Andrews, M. Barberio, J. Böker, F. Cardelli, J. L. Feugeas, M. Glesser, P. Nicolaï, L. Romagnani, M. Scisciò, M. Starodubtsev, O. Willi, J. C. Kieffer, V. Tikhonchuk, H. Pépin, L. O. Silva, E. d'Humières, and J. Fuchs, Sci. Rep. **7**, 16463 (2017).
10. L. Willingale, S. P. D. Mangles, P. M. Nilson, R. J. Clarke, A. E. Dangor, M. C. Kaluza, and J. Schreiber, Phys. Rev. Lett. **96**, 245002 (2006).
11. T. Esirkepov, M. Yamagiwa, and T. Tajima, Phys. Rev. Lett. **96**, 105001 (2006).
12. L. Willingale, S. P. Mangles, P. M. Nilson, R. J. Clarke, A. E. Dangor, M. C. Kaluza, A. G. Thomas, M. S. Wei, K. Krushelnick, and Z. Nahmudin, IEEE Trans. Plasma Sci. **36**, 1825 (2008).
13. F. Fiuza, A. Stockem, E. Boella, R. A. Fonseca, L. O. Silva, D. Haberberger, and C. Joshi, Phys. Rev. Lett. **109**, 215001 (2012).
14. N. P. Dover, N. Cook, O. Tresca, O. Ettlinger, C. Maharjan, M. N. Polyanskiy, and Z. Najmudin, J. Plasma Phys. **82**, 415820101 (2016).
15. C. A. Palmer, N. P. Dover, I. Pogorelsky, M. Babzien, G. I. Dudnikova, M. Ispiriyan, and Z. Najmudin, Phys. Rev. Lett. **106**, 014801 (2011).
16. D. Haberberger, S. Tochitsky, F. Fiuza, C. Gong, R. A. Fonseca, L. O. Silva, and C. Joshi, Nature Phys. **8**, 95 (2012).
17. O. Tresca, N. P. Dover, N. Cook, C. Maharjan, M. N. Polyanskiy, Z. Najmudin, and I. Pogorelsky, Phys. Rev. Lett. **115**, 094802 (2015).
18. W. L. Kruer, *The Physics of Laser Plasma Interactions* (Addison-Wesley, Reading, MA, 1988).
19. R. Dendy, *Plasma Physics: An Introductory Course* (Cambridge University Press, Cambridge, 1993).
20. L. I. Sedov, *Similarity and Dimensional Methods in Mechanics* (American Press Inc., New York, 1959).
21. Y. B. Zel'Dovich and Y. P. Raizer, *Physics of Shock Waves and High-Temperature Hydrodynamic Phenomena* (Academic Press Inc., New York, 1966).
22. P. L. Sachdev, *Shock Waves & Explosions* (CRC Press, New York, 2016).
23. C. Palmer, N. Dover, I. Pogorelsky, M. Streeter, and Z. Najmudin, J. Plasma Phys. **81**, 365810103 (2015).
24. Z. Najmudin, C. A. J. Palmer, N. P. Dover, I. Pogorelsky, M. Babzien, A. E. Dangor, G. I. Dudnikova, P. S. Foster, J. S. Green, M. Ispiriyan, D. Neely, M. N. Polyanskiy, J. Schreiber, P. Shkolnikov, and V. Yakimenko, Phys. Plasmas **18**, 056705 (2011).
25. D. Lamb, E. Harder, K. Weide, S. Feister, C. Walker, J. Truran, P. Tzeferacos, A. Dubey, N. Flocke, J. T.

https://doi.org/10.1017/hpl.2020.5 Published online by Cambridge University Press

Laute, and C. Graziani, "FLASH User's Guide Version 4.3", http://flash.uchicago.edu/site/flashcode/user_support/flash4_ug_4p3.pdf (2015).
26. S. K. Godunov, Mat. Sb. **89**, 271 (1959).
27. S. K. Godunov, A. V. Zabrodin, and G. P. Prokopov, Zhurnal Vychis. Mat. Mat. Fiz. **1**, 1020 (1961).
28. B. Van Leer, J. Comput. Phys. **32**, 101 (1979).
29. B. Van Leer and P. R. Woodward, *Proceedings of the TICOM Conference* (1979).
30. P. Colella and P. R. Woodward, J. Comput. Phys. **54**, 174 (1984).
31. P. MacNeice, K. M. Olson, C. Mobarry, R. De Fainchtein, and C. Packer, Comput. Phys. Commun. **126**, 330 (2000).
32. M. J. Berger and J. Oliger, J. Comput. Phys. **53**, 484 (1984).
33. M. J. Berger and P. Colella, J. Comput. Phys. **82**, 64 (1989).
34. D. DeZeeuw and K. G. Powell, J. Comput. Phys. **104**, 56 (1993).
35. Imperial College London CX1 cluster for high-performance computing, https://www.imperial.ac.uk/admin-services/ict/self-service/research-support/rcs/computing/high-throughput-computing (October 29, 2018).

https://doi.org/10.1017/hpl.2020.5 Published online by Cambridge University Press